J Solid State Electrochem (2009) 13:1613–1619
DOI 10.1007/s10008-008-0744-7

ORIGINAL PAPER

Preparation and electrochemical characterization of a new $NiMoO_4$ catalyst for electrochemical O_2 evolution

R. N. Singh · Madhu · R. Awasthi · A. S. K. Sinha

Received: 25 August 2008 / Revised: 8 November 2008 / Accepted: 12 November 2008 / Published online: 3 December 2008

Abstract The $NiMoO_4$ catalyst has been obtained by a precipitation method under a controlled pH condition and characterized ex situ by infrared, X-ray diffraction, Brunauer–Emmett–Teller (BET), and particle size, and in situ by cyclic voltammetry, impedance and steady-state anodic Tafel polarization techniques. Results show that $NiMoO_4$ has pure crystalline monoclinic phase with the crystallite size ~50 nm and the lattice constants, a= 9.597 Å, b=8.765 Å, c=7.667 Å, and β=114.22°. Values of the average particle size and BET surface area of the oxide powders are found to be 730 nm and 11.75 m^2/g, respectively. The oxygen evolution reaction follows the first-order kinetics with respect to OH^- concentration, the Tafel slope being ~70 mV.

Keywords Oxygen evolution · Electrocatalytic properties · Electrocatalysis · Mixed oxide

Introduction

Electroevolution and electroreduction of oxygen are technologically important reactions because they are used in many electrochemical systems related to energy conversion, such as water electrolysis, fuel cells, metal–air batteries [1–5], etc. However, the oxygen electrode reaction has a high overpotential in aqueous solutions, resulting in low energy efficiency [5]. Numerous electrocatalyst have been investigated to reduce the overpotential [5–7]. Among these, transition metal complex oxides belonging to spinel (Co_3O_4, $NiCo_2O_4$) [8–11] and perovskite ($LaNiO_3$, $LaCoO_3$) [12–17] structures are considered most promising ones and have been investigated extensively. The spinel-type mixed oxides have a general molecular formula AB_2O_4, in which A and B are transition metals, while the perovskite-type mixed oxides have the molecular formula ABO_3, in which A is a rare earth and B is a transition metal.

Very recently, Singh et al. [18] have reported the physicochemical and electrocatalytic properties of a new type of transition metal mixed oxides with compositional formula $MMoO_4$ (M=Co, Ni, or Fe). The oxides were prepared by thermal decomposition of mixed metal salts at 650 °C. All the three oxide catalysts were quite active for the oxygen evolution reaction (OER) and exhibited the Tafel slopes close to 40 mV. This result prompted us to prepare $NiMoO_4$ by a low temperature precipitation method so as to obtain pure and more homogeneous product with considerably enhanced specific surface area and examine its electrochemical and electrocatalytic properties in relation to the OER in an alkaline medium. Results of the investigation are reported in this paper.

R. N. Singh (✉) · Madhu · R. Awasthi
Department of Chemistry, Faculty of Science,
Banaras Hindu University,
Varanasi 221005, India
e-mail: rnsbhu@rediffmail.com

A. S. K. Sinha
Department of Chemical Engineering, Institute of Technology,
Banaras Hindu University,
Varanasi 221005, India

Experimental

Oxide preparation

The mixed oxide, $NiMoO_4$, was synthesized by precipitation from an aqueous solution of $Ni(NO_3)_2{\cdot}6H_2O$ (GR, Merck) and ammonium haptamolybdate (GR, Merck) [19].

For the purpose, the required amount of ammonium heptamolybdate was dissolved in 100 ml distilled water and maintained pH at ~5 and temperature at ~80–85 °C of the solution. To this, an aqueous solution of Ni $(NO_3)_2{\cdot}6H_2O$ (GR, Merck) was added, as per stoichiometric requirement, in a dropwise manner under stirred condition. When the addition of the metal nitrate solution was over, pH (~5) and temperature (80–85 °C) of the resulting solution were again maintained and kept as such for 5 min to complete the precipitation. The solution pH was maintained with the aid of ammonia and HNO_3 solutions. The precipitate was filtered, washed repeatedly with hot distilled water, dried in electrical furnace at ~100 °C overnight, crushed to fine particles, heated at 550 °C for 5 h, and again crushed and heated at 550 °C for 1 h to obtain the desired catalyst.

Structural and surface studies

The X-ray diffraction (XRD) powder pattern of the oxide catalyst was recorded on an X-ray diffractometer (Rigaku DMAX III) using Cu-K_α as radiation source (λ=1.542 Å). A Varian FTIR spectrometer (Model 3100) was used for recording the infrared (IR) spectra of the compound. The Brunauer–Emmett–Teller (BET) surface area of oxide powders was measured using a surface area analyzer (Micromeritics, USA, ASAP 2020 Model).The average particle size of powders of the oxide was measured using a particle size and shape analyzer ANKERSMTD Holland. Morphology of the compound has been studied by scanning electron micrograph (SEM, JEOL 840A).

Oxide-film electrode preparation

Ni plate (~1.5×1 cm) was used as conductive support for the oxide film preparation. Prior to use, the support was etched for 20 min in concentrated HCl, washed with double-distilled water, degreased in acetone, cleaned ultrasonically in double-distilled water, and then dried in air. Slurry was then prepared by mixing ~100 mg oxide powder with four to five drops of glycerol (GR, Merck) in Agate pastel mortar. The oxide slurry was coated on the pretreated Ni support, dried, and subsequently heated in an electrical furnace at 350 °C for 1.5 h. The coating procedure is repeated to obtain the catalyst film of the desired loading. An electrical contact with the oxide film was made as described previously [16].The loading of oxide films ranged between 2 and 4 mg cm^{-2}.

Electrochemical studies

A conventional three-electrode single-compartment Pyrex glass cell was used to carry out electrochemical investigation using electrochemical impedance system (EG &G, PARC, USA) provided with lock-in amplifier (Model 5210), a potentio-galvanostat (Model 273A), and P-4 COMPAQ computer. The reference and auxiliary electrodes were Hg/HgO/1 M KOH ($E°$=0.098 V vs standard hydrogen electrode) and pure Pt foil (~8 cm^{-2}), respectively. The reference electrode was connected to the cell solution through a Luggin capillary. All potential values, mentioned in the text, are given against this reference only. Cyclic voltammetry (CV) of the $NiMoO_4$ electrode in 1 M KOH has been carried out between 0.0 and +0.65 V, and the final voltammogram was recorded only after cycling it at the scan rate of 50 mV s^{-1} for 20 cycles. The electrochemical impedance spectroscopy (EIS) study of the electrode has been carried out with AC voltage amplitude of 10 mV. The frequency range used in the study was 0.1–10^4 Hz, and softwares employed were 'Power Sine' and 'ZSimpWin version 3.00'. 'M 352 Corrosion Analysis' software was used to perform the anodic Tafel polarization study. The procedure followed in the determination of IR_s-free Tafel plots (E vs log j) has

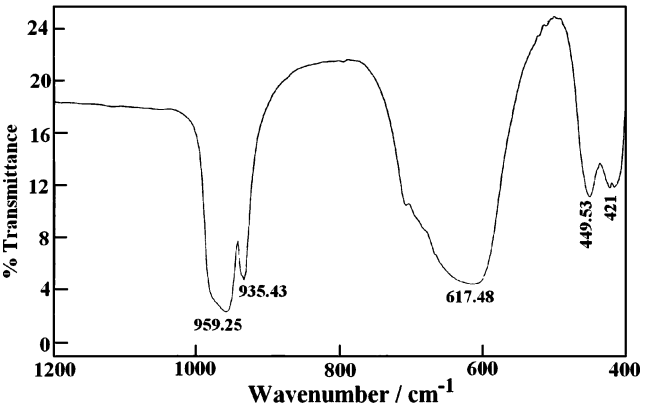

Fig. 1 IR spectrum of $NiMoO_4$ sintered at 550 °C for 6 h

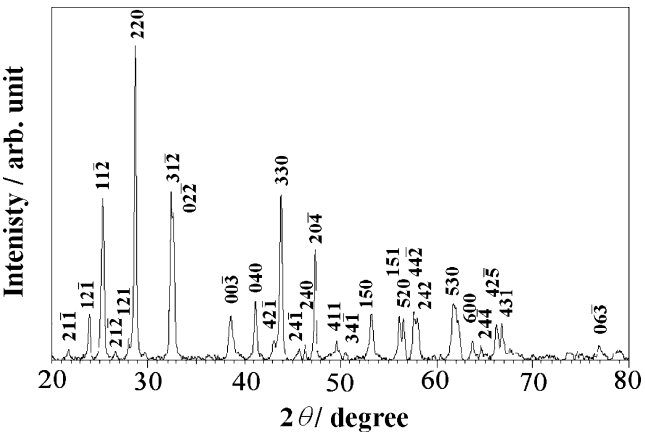

Fig. 2 XRD of $NiMoO_4$ sintered at 550 °C for 6 h

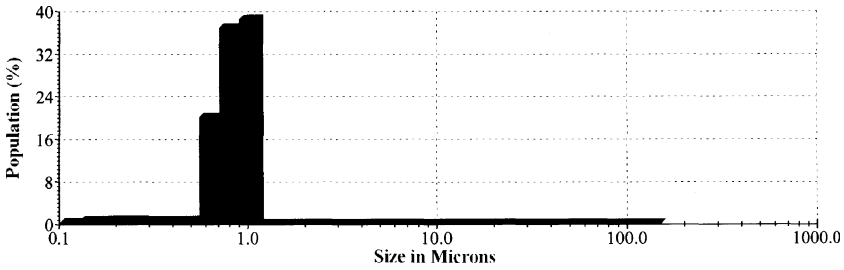

Fig. 3 A typical histogram of particle size, based on area density of the $NiMoO_4$

already been described elsewhere [17]. The IR_s was automatically compensated at an interval of 10 s using the current interrupt technique provided in electrochemical impedance system. All the electrochemical investigations have been made with triplicate electrodes at 25 °C.

Results and discussion

Structural and surface characterization

Infrared

IR spectrum of the oxide recorded in the region 1,200–400 cm^{-1} is shown in Fig. 1. This spectrum exhibits two broad peaks, at ~959 and ~617 cm^{-1}, and two narrow peaks, at ~935 and ~450 cm^{-1}. Similar absorption peaks were also found by Brito and Barbosa [19] and Mazzocchia et al. [20] for $NiMoO_4$, prepared from a mixed aqueous solution of $Ni(NO_3)\cdot 6H_2O$ and H_2MoO_4 by precipitation method. The three observed bands at ~959, ~935, and ~617 cm^{-1} are the characteristics of the α-phase of $NiMoO_4$ having a well-defined octahedral structure [21, 22].

X-ray diffraction

Figure 2 shows the XRD powder pattern of the compound recorded between $2\theta=20°$ and $2\theta=80°$. This figure demonstrates that the present precipitation method yields pure crystalline $NiMoO_4$ phase. The crystallite of oxide followed the monoclinic crystal geometry with unit cell dimensions a=9.597 Å, b=8.765 Å, c=7.667 Å, and β=114.22°. Values of the cell parameters have been estimated using a computer-based dhkl analysis program and found to be very close to those already given for $NiMoO_4$ in JCPDS file, 32-0692. An estimate of the crystalline size, based on the Scherrer formula [23, 24], was found to be ~50 nm. The most intense diffraction peak (220) was used for the determination of the crystallite size.

Particle size/Brunauer–Emmett–Teller/scanning electron microscopy

The mean particle size of powders of $NiMoO_4$ has been determined using a particle size and shape analyzer. The mean particle size based on area was 730 nm. A typical histogram for particle size of powders of $NiMoO_4$ is shown in Fig. 3. As seen from the density curve, the particle size

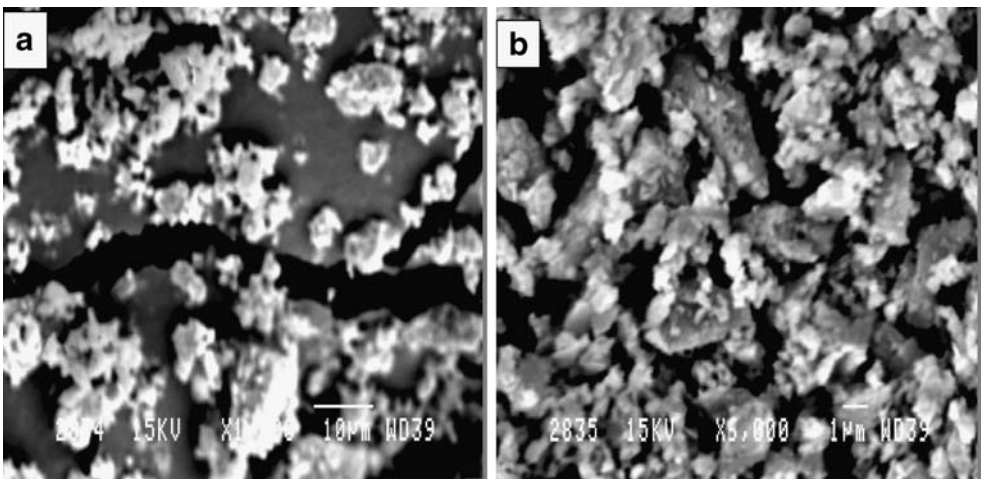

Fig. 4 SEM pictures of $NiMoO_4$ at magnifications (**a**) ×1,500 and (**b**) ×6,000

varies from 0.1 to 200 μm. The size range was divided into a number of segments, and the average was calculated using the formula

$$\text{Average size based on area} = \left(\sum x^2 \mathrm{d}N \Big/ \sum \mathrm{d}N\right)^{1/2},$$

where x is the mean length of the segment and dN is the number of particles (percent population) of size falling between that segment of size. The above statistical calculation was performed by the software of the analyzer. The BET surface area of the oxide was 11.75 $m^2\ g^{-1}$.

The SEM pictures of the compound at two magnifications (×1,500 and ×6,000) are shown in Fig. 4. This figure shows that the particles have irregular shape; however, the oxide surface looks porous.

Cyclic voltammetry

The CV of the $NiMoO_4$/Ni electrode, in the potential region from 0 to 0.65 V vs Hg/HgO, in 1 M KOH has been recorded (without interruption) at the scan rate of 50 mV s^{-1} for 25 cycles. The study has shown that the voltammogram gets almost stabilized after 20th cycle. Figure 5 represents CV curves of the electrode recorded between the 21st and 25th cycles only. Each curve, shown in Fig. 5, shows the formation of a pair of redox peaks, an anodic (peak potential, E_{pa}=~470 mV) and a corresponding cathodic one (peak potential, E_{pc}=~370 mV), prior to the onset of the OER.

It is known [7, 25] that an oxide film, obtained on a conductive support at low temperature, usually becomes hydrophilic in nature and that it undergoes rapid hydration in aqueous solution, resulting in wetting of the whole film thickness. However, this does not affect the stability of the oxide film practically. Thus, pure Ni, which is used as the support in the present investigation, may come under the electrolyte contact and produce oxidation–reduction peaks along with the oxidation–reduction current peaks of the $NiMoO_4$ film during the potential cycling condition. Therefore, to assess the contribution of the Ni support, cyclic voltammograms of pure Ni and of the $NiMoO_4$ film on Pt were also recorded under identical experimental conditions, and curves so obtained are reproduced in Fig. 6.

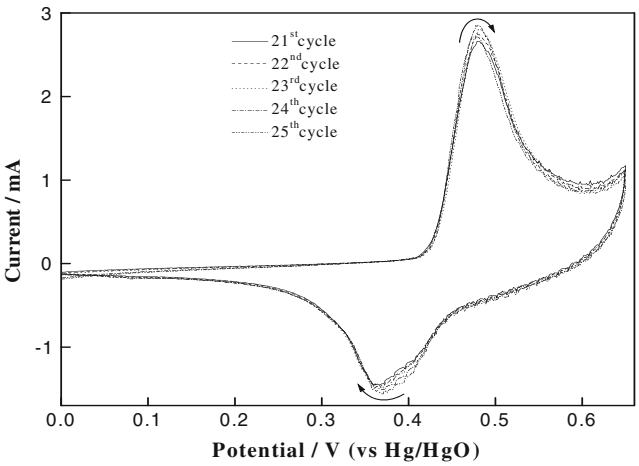

Fig. 5 Cyclic voltammograms of $NiMoO_4$/Ni electrode at the scan rate of 50 mV s^{-1} in 1 M KOH at 25 °C

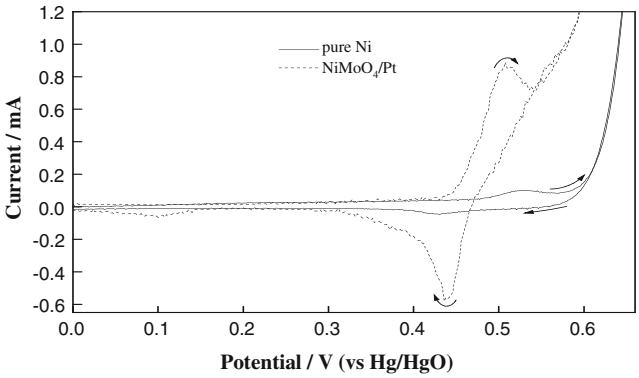

Fig. 6 Cyclic voltammograms of pure Ni and $NiMoO_4$/Pt electrodes at the scan rate of 50 mV s^{-1} in 1 M KOH at 25 °C

The observation in Fig. 6 shows that the oxide film obtained on Pt indicates an anodic (E_{pa}=526 mV) and a corresponding cathodic (E_{pc}=424 mV) peak. As Pt does not contribute any oxidation–reduction peak between 0 and 0.65 V, these peaks must have been originated from the oxide ($NiMoO_4$) overlayer only. Moreover, the voltammogram for pure Ni under identical conditions also exhibits a pair of redox peaks with E_{pa}=~510 mV and E_{pc}=~440 mV, which thereby substantiate the formation of the Ni(III)/Ni (II) redox couple, [26]. Thus, the results show that a pair of

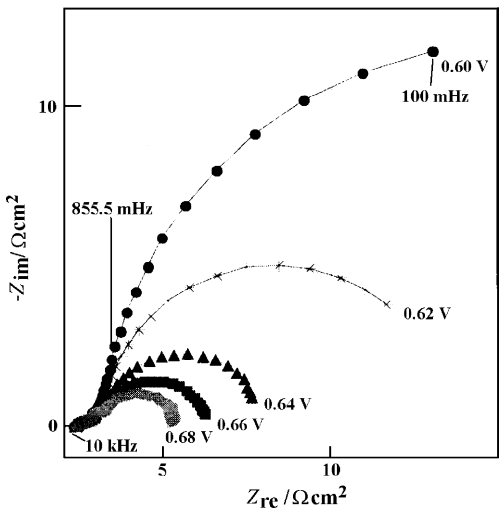

Fig. 7 Complex impedance diagrams for $NiMoO_4$/Ni electrode in 1 M KOH at varying potentials

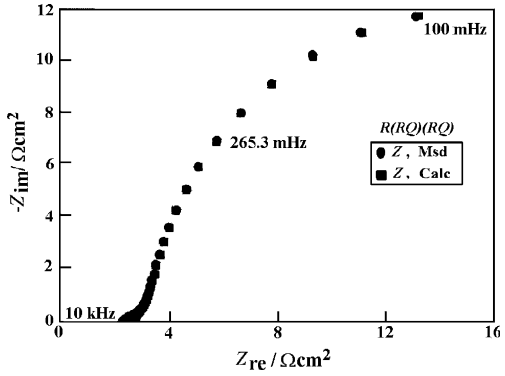

Fig. 8 Nyquist plots (experimental and simulated) for $NiMoO_4$/Ni electrode at 0.62 V in 1 M KOH

current peaks produced at the $NiMoO_4$ electrode surface, regardless of the nature of support, during the potential cycling condition is essentially due to the formation of the Ni(III)/Ni(II) redox couple. However, the observed low value of the formal redox potential (E°=420 mV) for the Ni (III)/Ni(II) redox couple formed on the $NiMoO_4$/Ni electrode surface compared to that formed on the $NiMoO_4$/Pt electrode surface or on pure Ni surface under identical experimental conditions may be attributed to the synergistic interaction between the metal support and the oxide overlayer. This effect may be caused due to the shift in electron density on Ni (in metal) toward the highly positively charged molybdenum (in oxide). Furthermore, the observed higher peak current values at the $NiMoO_4$/Ni electrode, compared to that at the $NiMoO_4$/Pt electrode, can be attributed to the oxidation of the Ni support (Fig. 6) during the potential cycling conditions.

Electrochemical impedance spectroscopy

Impedance measurements were carried out on the catalyst in 1 M KOH at five different potentials (0.60, 0.62, 0.64, 0.66, and 0.68 V). Before recording each EIS spectrum at a preselected DC potential, the electrode was first kept at this potential to equilibrate for 300 s. EIS spectra obtained at varying potentials are shown in Fig. 7. The complex impedance diagrams shown in Fig. 7 indicate the formation of two arcs, the first one at high frequency and the second one at low frequency. The high-frequency semicircle is relatively small and seems to be independent of potential. However, the diameter of low-frequency semicircle shrinks with increasing potential. This shows that the low frequency arc has been produced due to electroformation of oxygen [27], while the high frequency arc is caused due to the bulk conductivity of the oxide film, which seems to be potential independent.

It is reported [7, 28] that when an oxide thin-film electrode obtained at low temperature (~400 °C) is exposed with a liquid electrolyte, the latter compound wets instantaneously the total oxide surface. Therefore, the developed surface can be considered to act like a planar surface [29]. In order to simulate the impedance data, we therefore used a planar electrical equivalent circuit with the circuit description code, R_S (R_1Q_1) (R_2Q_2) (Fig. 8). In this circuit, parallel (R_1Q_1) combination takes into account the properties of bulk oxide, while parallel (R_2Q_2) combination is associated with the OER. Symbols R_s, R_1, and R_2 represent the solution, oxide film, and charge transfer resistances, respectively, and Q_1 and Q_2 represent constant phase elements (CPE) for the bulk oxide and the oxide/solution interface, respectively. In the proposed equivalent circuit, the two CPE have been used instead of pure capacitors (C) to obtain a better agreement between experimental and simulated data. The CPE is related to the impedance (Z_{CPE}) through the relation $Q = 1/Z_{CPE}(j\omega)^{\alpha}$, where $j=(-1)^{1/2}$ and α represents the deviation from the ideal behavior, being α=1 for perfect capacitors. Based on the proposed circuit model, EIS spectrum obtained agrees reasonably well with the experimental curve (Fig. 8). Estimates of the circuit parameters are shown in Table 1. Values of double-layer capacitance (C_{dl}) given in Table 1 were estimated using Eq. 1 [30].

$$Q_2 = (C_{dl})^{\alpha 2}\left[(Rs)^{-1}+(R_{ct})^{-1}\right]^{1-\alpha 2} \quad (1)$$

The above relation is used to compute the C_{dl} when the CPE is coupled with the charge transfer process. It is noteworthy that values of the capacitance shown in Table 1 are too high and that they are not the true C_{dl}. In fact, considerably enhanced values of the C_{dl} are obtained due to modification of the oxide/1 M KOH interface by adsorbed OH^- ions in the OER region [12].

Table 1 Values of the equivalent circuit parameters for $NiMoO_4$/Ni electrode in 1 M KOH

E/V	R_s/Ω cm^2	R_1/Ω cm^2	10^2Q_1/S s$^{\alpha}$ cm^{-2}	α_1	R_2/Ω cm^2	10^2Q_2/S s$^{\alpha}$ cm^{-2}	α_2	10^2C_{dl} /F cm^{-2}	R_F
0.60	2.22	1.63	19.02	0.37	24.56	8.11	0.98	7.82	~1,300
0.62	2.26	1.5	14.83	0.41	9.93	7.34	0.99	7.22	~1,200
0.64	2.26	1.47	11.99	0.42	4.37	7.16	0.99	6.99	~1,165
0.66	2.33	1.09	7.85	0.47	2.95	7.13	0.94	6.13	~1,020
0.68	2.37	1.26	10.85	0.43	1.87	7.59	0.96	6.83	~1,140

From Table 1, it is clear that the charge transfer resistance (R_2=R_{ct}) decreases, and hence the rate for the OER increases with the increase in potential. Values of the current density (j) at varying potentials were also estimated using the relation

$$R_{ct} = RT/nFj \quad (2)$$

where R, T, n, F, and j are molar gas constant (J K^{-1} mol^{-1}), temperature (K), number of electrons involved in reaction which is four, faraday constant, and apparent current density (A cm^{-2}), respectively. $j-E$ data thus obtained were expressed in form of the Tafel plot as shown in Fig. 9, which is found to be linear with a slope of ~69 mV for the OER at the $NiMoO_4$ electrode.

Values of the roughness factor, R_F (i.e., electrochemically active area) for the oxide electrode, shown in Table 1, are considerably high and appear to change little with potential in the OER region. Furthermore, R_s and R_1 values do not depend on potential practically. The R_F values given in Table 1 were estimated from the ratio of the C_{dl} of the oxide catalyst and the C_{dl} of a smooth oxide surface (i.e., 60 μF cm^{-2}) [13, 14].

Electrocatalytic activity

To confirm the result of the EIS study, the IR_s-compensated steady-state anodic Tafel polarization curve (E vs log j) for $NiMoO_4$ electrode was determined at a scanning rate of 0.2 mV s^{-1} and shown in Fig. 10. The curve shown in Fig. 10 shows a Tafel slope (b) ~70±1 mV at low overpotentials. This value of b is quite close to that obtained from the impedance study (~69 mV). Values of the apparent current density (j) were 10, 50, and 100 mA cm^{-2} while that of the true current density (j_t=j/R_F) were 8.58, 42.92, and 85.84×10^{-3} mA cm^{-2} at E=0.676, 0.738, and 0.79 V, respectively.

To determine the reaction order (p) in [OH^-], E vs log j curves for the electrocatalyst were determined at varying

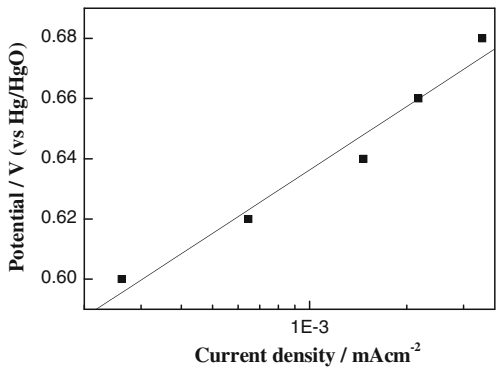

Fig. 9 Tafel plot for O_2 evolution on $NiMoO_4$/Ni electrode based on $j-E$ data, obtained from the impedance measurements

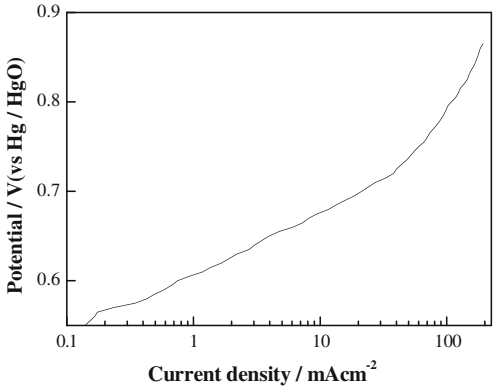

Fig. 10 Tafel plot for O_2 evolution on $NiMoO_4$ electrode in 1 M KOH

KOH concentrations, maintaining the ionic strength of medium constant (μ=2.0) (Fig. 11). The order was then computed from the slope of the linear plot, log j vs log [OH^-], constructed at a constant potential and found to be 1.2.

Results of the electrode kinetic parameters (b and p) obtained in the present investigation are similar to those already reported on Co-based spinels [11, 31–37] and Co-based perovskites [12, 14, 15]. However, these are significantly different from those (b ≈ 40 mV, p ≈ 2 at low overpotentials) recently reported [18] for the same oxide ($NiMoO_4$), obtained by thermal decomposition method. This difference in the electrode kinetic parameters can be attributed to the method, conditions, and starting materials employed in the preparation of the catalyst [38, 39]. In fact, all the three parameters were different in preparation of the oxide catalyst, $NiMoO_4$, of the present study.

The observed values of b and p for the OER on $NiMoO_4$ in the present study indicate a mechanism, which involves

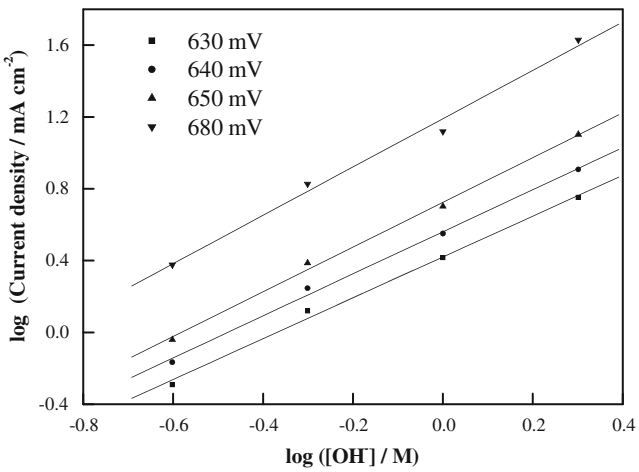

Fig. 11 Log j vs log [OH^-] plots for O_2 evolution on of $NiMoO_4$/Ni electrode at a constant potential (from Fig. 10)

the discharge of a molecule of OH^- with the formation of the adsorbed OH intermediate as a fast step and subsequent electrochemical interaction between the surface adsorbed intermediate and OH^- as the rate-determining step. Under Temkin adsorption conditions ($0.2<\theta_T<0.8$, where θ_T being the total surface coverage by adsorbed intermediates and products), the proposed mechanism would produce $b \approx 60$ mV and $p \approx 1.5$, which are in close agreement with the experimental values ($b=69$ mV and $p=1.2$). Similar mechanisms for the OER have already been suggested in literature [12, 16].

Conclusion

The study shows that the present precipitation method produces pure nanosized crystallites of $NiMoO_4$ following the monoclinic crystal geometry. The electrocatalytic activity of this new oxide catalyst toward OER is reasonably good. Values of the electrode kinetic parameters are found to be almost similar to those of Co-based spinel/perovskite oxides.

Acknowledgments One of the authors thanks the Council of Science and Industrial Research (CSIR), Government of India for the award of a Junior Research Fellowship (JRF) to carry out the investigation. Authors also thank the CSIR for the financial support of the work through a research project (Ref. no. 01(2033)/06/EMR-II).

References

1. Chebotareva N, Nyokong T (1997) Electrochim Acta 42:3519. doi:10.1016/S0013-4686(97)00033-9
2. Vielstich W (2003) J Braz Chem Soc 14:503. doi:10.1590/S0103-50532003000400003
3. Mao L, Zhang D, Sotomura T, Nakatsu K, Koshiba N, Ohsaka T (2003) Electrochim Acta 48:1015. doi:10.1016/S0013-4686(02)00815-0
4. Huang H, Zhang W, Li M, Gan Y, Chen J, Kuang Y (2005) J Coll Interf Sci 284:593. doi:10.1016/j.jcis.2004.10.067
5. O'Sullivan EJM, Calvo EJ (1987) Reaction at metal oxide electrodes. In: Compton RG (ed) Comprehensive chemical kinetics: electrode kinetics reactions,. vol. 27. Elsevier, Amsterdam, pp 247–360
6. Trasatti S, Lodi G (1981) Oxygen and chlorine evolution at conductive metallic oxide anodes. In: Trasatti S (ed) Electrodes of conductive metallic oxides, part B. Elsevier, Amsterdam, pp 521–625
7. Trasatti S (1994) Transition metal oxides: versatile materials for electrocatalysis. In: Lipkowski J, Ross PN (eds) Electrochemistry of novel materials. VCH, New York, pp 207–295
8. Tavares AC, Bochatay L, da Silva Pereira MI, da Costa FM (1996) Electrochim Acta 41:1953. doi:10.1016/0013-4686(95)00483-1
9. Tavares AC, Cartaxo MAM, da Silva Pereira MI, Costa FM (1999) J Electroanal Chem 464:187. doi:10.1016/S0022-0728(99)00018-2
10. Rios E, Gautier J-L, Poillerat G, Chartier P (1998) Electrochim Acta 44:1491. doi:10.1016/S0013-4686(98)00272-2
11. Svegl F, Orel B, Grabec-Svegl I, Kaucic V (2000) Electrochim Acta 45:4359. doi:10.1016/S0013-4686(00)00543-0
12. Bockris JO'M, Otagawa T (1983) J Phys Chem 87:2960. doi:10.1021/j100238a048
13. Bockris JO'M, Otagawa T (1984) J Electrochem Soc 131:290. doi:10.1149/1.2115565
14. Tiwari SK, Chartier P, Singh RN (1995) J Electrochem Soc 142:148. doi:10.1149/1.2043854
15. Tiwari SK, Singh SP, Singh RN (1996) J Electrochem Soc 143:1505. doi:10.1149/1.1836670
16. Singh RN, Koenig J-F, Poillerat G, Chartier P (1990) J Electrochem Soc 137:1408. doi:10.1149/1.2086682
17. Singh RN, Sharma T, Singh A, Anindita, Mishra D, Tiwari SK (2008) Electrochim Acta 53:2322. doi:10.1016/j.electacta.2007.09.047
18. Singh RN, Singh JP, Singh A (2008) Int J Hydrogen Energy 33:4260. doi:10.1016/j.ijhydene.2008.06.008
19. Brito JL, Barbosa AL (1997) J Catal 171:467. doi:10.1006/jcat.1997.1796
20. Mazzocchia C, Aboumrad C, Diagne C, Tempeste E, Herrmann JM, Thomas G (1991) Catal Lett 10:181. doi:10.1007/BF00772070
21. Maldonado-Hodar FJ, Palma Madeira LM, Farinha Portela M (1996) J Catal 164:399. doi:10.1006/jcat.1996.0396
22. Martin-Aranda RM, Portela MF, Madeira LM, Freire F, Oliveira M (1995) Appl Catal A127:201
23. Fradette N, Marsan B (1998) J Electrochem Soc 145:2320
24. Fatih K, Marsan B (1997) Can J Chem 75:1597
25. Singh RN, Singh JP, Singh NK, Lal B, Chartier P, Koening JF (2000) Electrochim Acta 45:1911. doi:10.1016/S0013-4686(99)00413-2
26. Anitha KL, Pandey JP, Singh RN (1993) Int J Hydrogen Energy 18:467. doi:10.1016/0360-3199(93)90002-R
27. Palmas S, Ferrara F, Vacca A, Mascia M, Polcaro AM (2007) Electrochim Acta 53:400. doi:10.1016/j.electacta.2007.01.085
28. Singh RN, Tiwari SK, Singh SP, Singh NK, Poillerat G, Chartier P (1996) J Chem Soc Faraday Trans 92:2593. doi:10.1039/ft9969202593
29. Singh RN, Singh A, Mishra D Anindita, Chartier P (2008) J Power Sources 185:776. doi:10.1016/j.jpowsour.2008.07.078
30. Brug GJ, Van den Eeden ALG, Rehbach MS, Sluyters JH (1984) J Electroanal Chem 176:275. doi:10.1016/S0022-0728(84)80324-1
31. Chi B, Jianbao L, Xiaozhan Y, Hong L, Ning W (2005) Electrochim Acta 50:2059. doi:10.1016/j.electacta.2004.09.014
32. Hamdani M, Pereira MIS, Douch J, Ait Addi A, Berghoute Y, Mendonca MH (2004) Electrochim Acta 49:1555
33. Rasiyah P, Tseung ACC (1983) J Electrochem Soc 130:2384. doi:10.1149/1.2119592
34. Rasiyah P, Tseung ACC (1983) J Electrochem Soc 130:365. doi:10.1149/1.2119712
35. Singh RN, Pandey JP, Singh NK, Lal B, Chartier P, Koenig JF (2000) Electrochim Acta 45:1911. doi:10.1016/S0013-4686(99)00413-2
36. Rios E, Chartier P, Gautier JL (1999) Solid State Sci 1:267. doi:10.1016/S1293-2558(00)80081-3
37. Singh NK, Singh JP, Singh RN (2002) Int J Hydrogen Energy 27:895. doi:10.1016/S0360-3199(01)00193-8
38. Iwakura C, Honji A, Tamura H (1981) Electrochim Acta 26:1319 doi:10.1016/0013-4686(81)85116-X
39. Garavaglia R, Mari CM, Trasatti S (1983) Surf Technol 19:197. doi:10.1016/0376-4583(83)90024-9